

Failure Mode and Degradation Analysis of a Commercial Sodium-Ion Battery With Severe Gassing Issue

Sebastian Klick^{+, [a, b, c]} Hendrik Laufen^{+, *[a, b, c]} Moritz Schütte,^[a, b, c] Bowen Qian,^[a, c] Katharina Lilith Quade,^[a, b, c] Christiane Rahe,^[a, b, c] Matthieu Dubarry,^[d] and Dirk Uwe Sauer^[a, b, c, e]

Sodium-ion batteries offer a promising alternative to lithium-ion batteries by addressing ecological and economic challenges. However, to assess the applicability of these cells for different sectors, understanding aging behavior, including degradation modes, is crucial. This work presents a comprehensive aging analysis of 67 commercial sodium-ion batteries under various temperatures, C-rates, and depths of discharge. We analyzed the initial cell-to-cell variance and the aging trajectories regarding capacity fade and resistance increase. We demonstrated that the cycling rate does not significantly influence the aging trajectories, whereas smaller depths of discharge significantly reduce degradation. The degradation gradients for 25°C and 40°C were similar; for -10°C, we observed rapid capacity

fading that can be attributed to irreversible sodium plating. Furthermore, we identified the degradation modes for four different aging categories. Since some aging tests stopped due to gas-induced current interrupt device triggering at low current rates and states of charge, we proposed two hypotheses for the gassing under specific conditions, suggesting inadequate gas consumption in cathode-electrolyte side reactions or solid electrolyte interphase instability as potential causes. Overall, this work provides a valuable in-depth analysis of the aging behavior of a commercial sodium-ion battery as a function of temperature, C-rate, and depth of discharge, with data made available for further research.

Introduction

The tremendous success of lithium-ion batteries (LIBs) as energy storage for different sectors is continuously accompanied by discussions about their ecological impact, economic development, and ethical circumstances. Facing the ecological and

ethical debate about cobalt, it has been argued that even when considering battery recycling, there are insufficient resources to meet the demand.^[1] Volatile raw material prices for cobalt^[2-4] as well as the dependency on the political and economic stability in the mining countries causing uncertain and rising prices. Shifting the attention towards sodium-ion batteries (SIBs) might offer a solution for the aforementioned issue due to the possibility of using less scarce materials for the positive electrode and the abundance of sodium.^[5] Requiring similar production processes and machines as their lithium-based counterparts^[6] and the great transferability of characterization methods, SIBs clearly indicate a strong drop-in potential for LIBs.^[7]

However, selecting a SIB for an application requires more than a drop-in potential rather than an extensive aging study revealing the cell chemistry's true potential. Systematic aging studies on SIBs beyond small lab formats are rare. He et al.^[8] analyzed a commercial cell optimized for high power applications using prussian blue analogs for both negative electrode (NE) and positive electrode (PE). This cell provides exceptionally high cycle life (>40,000 cycles), but has a low energy density of 10.3 Wh kg⁻¹ at pack level.^[8] Another aging study with cylindrical 18650 cells using NVPF as a cathode active material has been reported in Ref. [9]. That study reported higher cycle life at higher C-rates and very limited calendar life at high State of Charges (SOCs).^[9] Having characterized one of the first commercially available SIBs in our previous work,^[7] the cell showed a great current rate (C-rate) capability and its initially conducted vestigial aging study indicated promising cyclic lifetime. But applying the cell's maximum allowed charging and

[a] S. Klick,⁺ H. Laufen,⁺ M. Schütte, B. Qian, K. L. Quade, Dr. C. Rahe, Prof. D. U. Sauer
Chair for Electrochemical Energy Conversion and Storage Systems, Institute for Power Electronics and Electrical Drives (ISEA), RWTH Aachen University, Campus-Boulevard 89, Aachen, 52074, Germany
E-mail: batteries@isea.rwth-aachen.de
Homepage: <https://www.carl.rwth-aachen.de>

[b] S. Klick,⁺ H. Laufen,⁺ M. Schütte, K. L. Quade, Dr. C. Rahe, Prof. D. U. Sauer
Juelich Aachen Research Alliance, JARA-Energy, Jülich, 52425, Germany

[c] S. Klick,⁺ H. Laufen,⁺ M. Schütte, B. Qian, K. L. Quade, Dr. C. Rahe, Prof. D. U. Sauer
Center for Ageing, Reliability and Lifetime Prediction of Electrochemical and Power Electronic Systems (CARL), RWTH Aachen University, Campus-Boulevard 89, Aachen, 52074, Germany

[d] Dr. M. Dubarry
University of Hawaii at Manoa, Hawaii Natural Energy Institute, 1680 East West Road, POST109, Honolulu, HI, 96815, USA

[e] Prof. D. U. Sauer
Helmholtz Institute Münster (HIMS), IMD-4, Forschungszentrum Jülich, Jülich, 52425, Germany

^{††} These authors contributed equally.

 Supporting information for this article is available on the WWW under <https://doi.org/10.1002/batt.202400546>

 © 2024 The Author(s). *Batteries & Supercaps* published by Wiley-VCH GmbH. This is an open access article under the terms of the Creative Commons Attribution License, which permits use, distribution and reproduction in any medium, provided the original work is properly cited.

discharging current resulted in activation of the current interrupt device (CID).^[7]

Driven by these observations, this work outlines an extensive aging study of the cell used in Laufen et al.^[7] Enriched by an international collaboration, this work profits from the aging analysis methodologies proposed by Dubarry et al.^[10–13] Providing insights on the cell to cell variations, the capacity fade, and the resistance increase, the degradation modes of those SIBs are thoroughly analyzed using these methodologies. Analyzing the activation of the CID is closing the discussion, bridging to a final conclusion.

Experimental

Investigated Cell

The cell investigated in this work is a 1.2 Ah 18650 cell obtained from Shenzhen Mushang Electronics Co., Ltd. An overview of the cell properties based on the specifications given by the manufacturer and additional electrical tests and post-mortem analysis was provided in Laufen et al.^[7]

According to the data sheet, the nominal capacity of the cell at a 0.5 C discharge within the given voltage window of 1.5–3.8 V at 25 °C is 1.25 Ah. The minimum capacity of the cell under the same conditions is given as 1.2 Ah. Based on results of the previous publication by Laufen et al.^[7] a nominal capacity of 1.2 Ah was used for the analysis in this work. The nominal voltage of the cell is given as 3.0 V. The operating voltage window for the cell is given as 1.5–3.8 V. The standard charging procedure was a 0.5 C constant current (CC) charge with a subsequent constant voltage (CV) phase terminated at 0.05 C (60 mA). The possible C-rates reached up to 5 C and 8 C for the charge and discharge process, respectively.

Aging Conditions

Investigating the aging behavior of the aforementioned SIB (c.f. Investigated Cell) led to 23 different aging conditions analyzed in this work. An overview of the cyclic and calendaric aging conditions is given in Table 1.

Two temperatures were chosen close to the operating limits. The lowest temperature of –10 °C in this work was chosen to analyze the cells' potential to be utilized in cold regions. Analyzing the cells' behavior at a temperature of 50 °C intended to gain insights on potential utilization in temperature intense industrial applications or applications with direct or prolonged exposure to sunlight.

Table 1. Overview of cyclic and calendaric aging conditions. Detailed definitions of the test procedures for each cell used in this work can be found in the supplemental information in Table S1 and Table S4.

Overview of aging conditions

Test ID	Temperature in °C	DOD in %	C-rate charge	C-rate discharge
CYC T-10 DOD80 1C1C	–10	80	1	1
CYC T-10 DOD100 0.5C0.5C	–10	100	0.5	0.5
CYC T-10 DOD100 1C1C	–10	100	1	1
CYC T-10 DOD100 2C2C	–10	100	2	2
CYC T25 DOD20 2C2C	25	20	2	2
CYC T25 DOD80 2C2C	25	80	2	2
CYC T25 DOD100 1C1C	25	100	1	1
CYC T25 DOD100 2C2C	25	100	2	2
CYC T40 DOD20 2C2C	40	20	2	2
CYC T40 DOD80 2C2C	40	80	2	2
CYC T40 DOD100 1C1C	40	100	1	1
CYC T40 DOD100 2C2C	40	100	2	2
CYC T50 DOD80 2C2C	50	80	2	2
CYC T50 DOD100 0.5C0.5C	50	100	0.5	0.5
CYC T50 DOD100 1C1C	50	100	1	1
CYC T50 DOD100 2C2C	50	100	2	2
CYC RT DOD100 1C1C	RT	100	1	1
CYC RT DOD100 3C1C	RT	100	3	1
CYC RT DOD100 3C8C	RT	100	3	8
CYC RT DOD100 5C1C	RT	100	5	1
CYC RT DOD100 5C8C	RT	100	5	8

Test ID	Temperature in °C	SOC in %
CAL T25 SOC100	25	100
CAL T40 SOC100	40	100

Aiming at identifying degradation modes of the SIB under application-related conditions, cyclic tests at a constant temperature of 25 °C and 40 °C were conducted. Different depth of discharges (DODs) and C-rates were applied to investigate their impact on cell degradation. All cyclic experiments executed at a constant temperature were operated in a climate chamber (BINDER MK53). The cycling test procedures were executed on BaSyTec CTS LAB 3A using the software BaSyTec Batterietestsoftware V6.2.34.0/BDE. Limited to a maximum C-rate of 2 C by the battery cycler, additional cyclic tests were conducted at room temperature (RT) (without climate chamber; temperature can vary between 20–23 °C) on a Neware BTS-4000 Series 5 V6 A and BTS-4000 Series 5V12A using the software BTS8.0.0.484.

The tests executed at RT allowed to analyze the influence of charging rates up to 5 C and discharging rates up to 8 C. Especially, investigating such elevated charging rates served the purpose of providing insights on whether this SIB technology fits in high-power applications like railroads.

In addition to the cyclic tests, calendaric tests at two different temperatures (25 °C and 40 °C) at a SOC of 100% were conducted. This test aimed at revealing the cells' potential for applications such as uninterruptible power supply, at which the cells are maintained at a fully charged state over years.

Detailed definitions of the test procedures for each cell used in this work can be found in the Supporting Information in Tables S1 and S4.

Half Cells

A classic method for determining the half-cell open-circuit potential (OCP) of the electrode material versus Na/Na⁺ involves constructing a coin cell with a sodium electrode.^[14–16] To avoid the influence of the electrode's backside on the coin cell's performance, a single-side coated working electrode was used. Thus, a double-side coated electrode was harvested from the cylindrical cell (referred to as full-cell in the following) and mechanically decoated on one side by scraping off the coating. The cell was discharged to 1.5 V before the cell opening. The assembly of these coin cells as well as the cell opening was conducted under an inert argon atmosphere in a glovebox (MBRAUN LABstar, with O₂ concentration <0.5 ppm and H₂O concentration <0.5 ppm).

The basic setup of the constructed coin cells in this work included a CR2032 housing, a spacer, a spring, a sodium metal chip (diameter 15.6 mm, AOT Battery, 30 μm aluminum layer for support and current collector, and a 420 μm sodium layer), a separator (diameter 17 mm, Whatman GF/C), electrolyte (90 μL, 1.2 M NaPF₆ in EC:PC 1:1 by weight), and a single-side coated electrode (diameter 16 mm) harvested from a full-cell.

The coin cell had a nominal capacity of 3.0 mAh within the full-cell voltage limits. The voltage of the NE and PE half-cell were measured applying a constant charging current of C/50 (60 μA). The voltage limits for the NE coin cell cycling were set from 0.01 V to 1.5 V without any rest phases between charge and discharge cycles. The voltage limits for the PE coin cell cycling were set from 2.2 V to 3.9 V without any rest phases between charge and discharge cycles.

Preparation of Incremental Capacity and Differential Voltage

Throughout this work the incremental capacity (IC) and differential voltage (DV) curves were used to analyze the aging behavior of the cells. This section provides a brief information how the IC and DV curves were derived.

For the full cell data, the IC and DV curves were derived by gathering the capacity or voltage elapsed after a set step (4 mV for IC, 1 mAh for DV) from a smoothed voltage curve (MatLab© "smooth" function with a factor of 500). For the half-cell data, steps of 2 mV and 0.1% with a smoothing factor of 750 were used for IC and DV.

Results

Cell to Cell Variations

For every new batch of cells, and especially with a new chemistry with limited production, it is essential to first characterize cell-to-cell variations^[10,17,18] in order to ensure that the variations observed throughout this study were induced by the different aging conditions and not by initial variations. Following the methodology proposed in Refs. [10] and [11], three attributes to cell-to-cell variations were quantified using the formation cycles. The three attributes were the cells maximum capacity, rate capability, and polarization. Quantifying these three parameters allowed to characterize the overall capacity versus C-rate relationship for the batch with information on the three main regions with material, diffusion, and polarization limitations.^[11] Figure 1 presents the results of this initial cell-to-cell variation analysis with the distribution of capacities at low C-rate and high C-rate (C/20 and C/2 respectively), their rate capability estimated as the ratio of the capacities at low and high C-rate, and their resistance calculated from the initial internal resistance (IR) drop for the high C-rate discharge. Looking at the capacity first, Figure 1a, the distribution at low and high C-rate both in charge and discharge was normal with around at 1240 mAh for C/20 and 1180 mAh for C/2, all with a 8 mAh standard deviation. The correlations between the charge and the discharge capacities and between the low and high C-rate capacities were 99% and 86% respectively which indicates that the performance is consistent between cells. This is also reflected on the rate capability, Figure 1b which was found to be of 95% both in charge and discharge with a skewed distribution and a longer tail towards the higher rate capabilities. Figure 1c presents the distribution of resistances where a bimodal distribution can be observed with a mode around 30 mΩ Ah⁻¹ and another one around 70 mΩ Ah⁻¹. Figure 1d summarizes the cell-to-cell variations information using a 3D plot^[11] with the inner full line, dashed, and dotted cubes representing the extend of a one, two, and three σ spread around the mean respectively. All the data was found to be within 2σ for all three attributes which indicates that no outliers were identified and that the cell-to-cell variations were overall rather small.

In addition to the traditional cell-to-cell variations, a closer analysis of the voltage response of the cell can bring additional information.^[12] This is to verify that the electrochemical reactions are proceeding normally and that no cell has a different electrochemical behavior. Figure 2 presents the voltage response of the cells at low (Figure 2a, c, and e) and high C-rate (Figure 2b, d, and e) with the voltage versus capacity

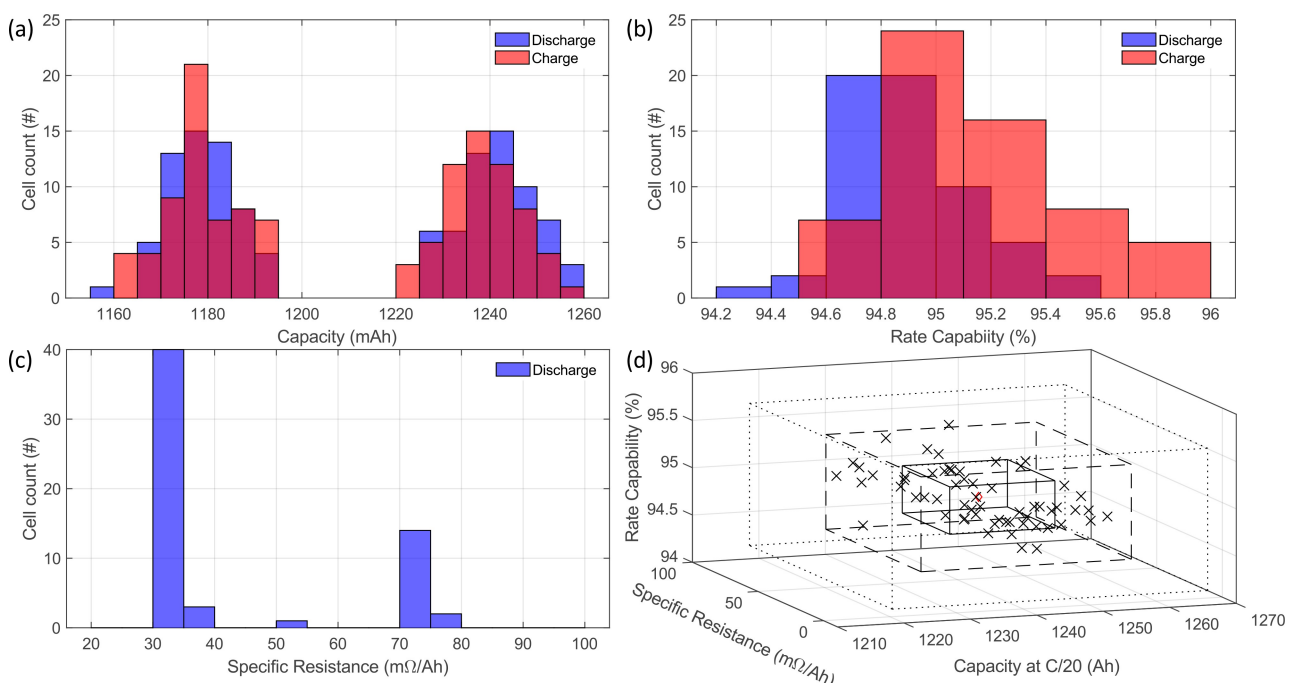


Figure 1. Distribution of (a) the initial cell capacities for both C/20 and C/2 charges and discharges [mean C/2 discharge: 1179 mAh; std. C/2 discharge: 7 mAh; mean C/2 charge: 1179 mAh; std. C/2 charge: 8 mAh], (b) the rate capability in charge and discharge [mean discharge: 94.9%; std. discharge: 0.3%; mean charge: 95.2%; std. charge: 0.3%], and (c) the resistance [mean discharge: $43.7 \text{ m}\Omega \text{ Ah}^{-1}$; std. discharge $18.1 \text{ m}\Omega \text{ Ah}^{-1}$]. (d) 3D visualization of the spread of cell-to-cell variations.

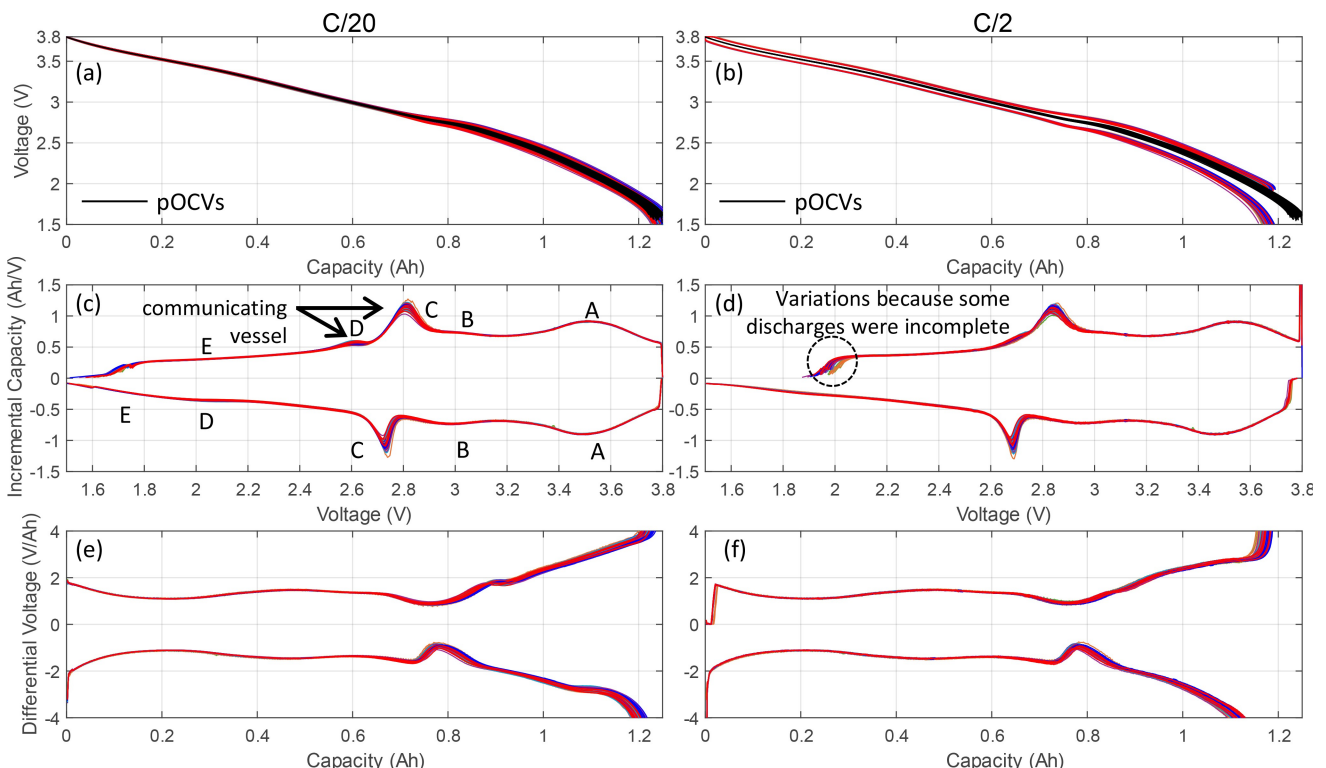


Figure 2. Initial voltage response at C/20 (left column) and C/2 (right column) for the 60 cells studied in this work with (a, b) the voltage vs. capacity curves, (c, d) the incremental capacity curves, and (e, f) the differential voltage curves.

curves (a,b), the IC responses (c,d), and the DV responses (e,f). The pseudo-open circuit voltage (pOCV) curves for all 60 cells,

calculated from the average of the C/20 charge and discharge curves, is also provided in black in Figure 2a,b. Overall, there is

little differences between the cells and all charge, discharge, and pOCV curves are all rather similar. Nonetheless, there are a few interesting things to note. For the low C-rate curves (left column), some small differences are observable on the IC curves. The electrochemical response of the cells consists of five main features with, from high to low voltage, two very broad peaks (A and B), a sharp peak (C), an asymmetric peak (D) broader in discharge than in charge, and a shoulder (E) at low voltages. The main difference between the cells were observed on peaks C and D with some communicating vessel effect with cells having a more intense peak C having a lower peak D and inversely. For the high C-rate curves (right column), there seems to be some kinetic limitations at the end of discharge, Figure 2b, as the discharge curves deviate a lot from the pOCV curves at low states of charge. Looking at their IC curves in charge, it can also be seen that the beginning of charge point is varying a little. This is induced by the previous discharge being incomplete as no residual capacity step was implemented to control the state of the cell at beginning of charge.

Capacity Fade

This section presents the capacity fade for various aging conditions. We start by comparing capacity fade during cyclic aging with different charge and discharge rates at room temperature.

Capacity fade was analyzed based on both the capacity obtained during cycling and the reference performance tests (RPTs). For calendar aging only results from the RPTs were available. The RPT for each cell contained a 0.5 C discharge capacity test, a 0.05 C discharge and charge step to obtain the quasi open-circuit-voltage (qOCV), and pulse tests. The detailed definition of the RPT for tests cycled in a climate chamber (-10°C , 25°C , 40°C , and 50°C) can be found in Table S5. For the cells cycled at RT, the RPT is part of the cycling procedure and can be found in Tables S17 to S22. The RPT for the calendaric tests is listed in Table S23.

Room Temperature Cycling

The trajectory of the capacity as measured during cycling at room temperature for different C-rates is displayed in Figure 3. An initial increase of capacity was observed, except for cells cycled with an 8 C discharge rate. This was followed by a declining capacity for all cells. Almost all tests were stopped due to a premature cell failure: As mentioned in Laufen et al.^[7] the CID was triggered after prolonged cycling. One exception was the cell cycled with 5 C/8 C which showed a lower capacity and rapid capacity decay during the first 400 cycles. This cell continued cycling until 2000 cycles. Its capacity decreased steadily and was below 0.7 Ah after 2000 cycles, as displayed in Figure 3. This cell differed from the others before the start of cycling, as its cell voltage was below 3.0 V (measured 2.89 V).

A comparison between the different C-rates shows that cells cycled with high charging rates exhibit a similar initial aging

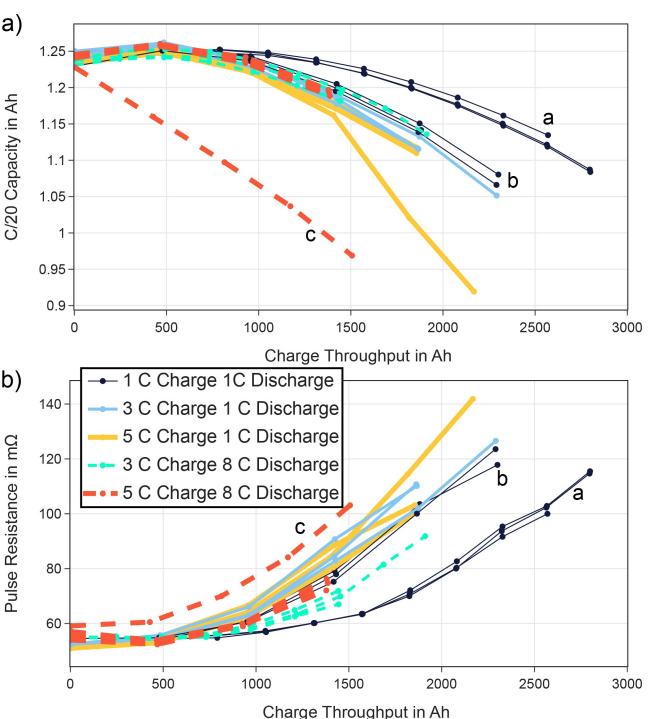


Figure 3. a) Capacity decay for cells cycled with different C-rates at room temperature. b) Resistance increase for the same cells. Cells cycled with 1 C charge and discharge marked with "a" underwent a C/5 cycle after 10 cycles, while this frequency was reduced to one C/5 cycle after 100 cycles for cells marked with "b". "c" marks the outlier cell which has a lower initial voltage.

trajectory but the CID is triggered in the order of the charge current: Cells charged with 5 C stopped after a charge throughput of roughly 1400 Ah, with one outlier which was stopped manually due to an abnormal capacity fade. Cells charged with 3 C last longer and achieved a total charge throughput just short of 1900 Ah. For cells charged with 1 C, two slightly different charging protocols were used resulting in different lifetimes. An increased frequency of RPTs and higher number of low-current cycles in group a (as marked in Figure 3) resulted in reduced capacity fade, and increased the charge throughput until the last RPT to about 2570 compared to 2300 for the longest lasting cell of group b. To investigate the influence of the discharge C-rate, cells were charged with 3 C and 5 C and discharged with 8 C. This resulted in a minor decrease in capacity fade.

Influence of Temperature and C-Rate on Capacity Fade

Figure 4 shows the capacity obtained from the RPTs as well as the pulse resistances R_{Pulse} for cells cycled with different C-rates and DODs at different temperatures. Figure 4 shows that capacity faded rapidly for cells cycled at -10°C indicating poor low temperature performance.

At 25°C cells performed best with a charge throughput in the range of 2120–2220 Ah until the CID of cells cycled with 2 C was triggered. The remaining tests at 25°C with 100% DOD

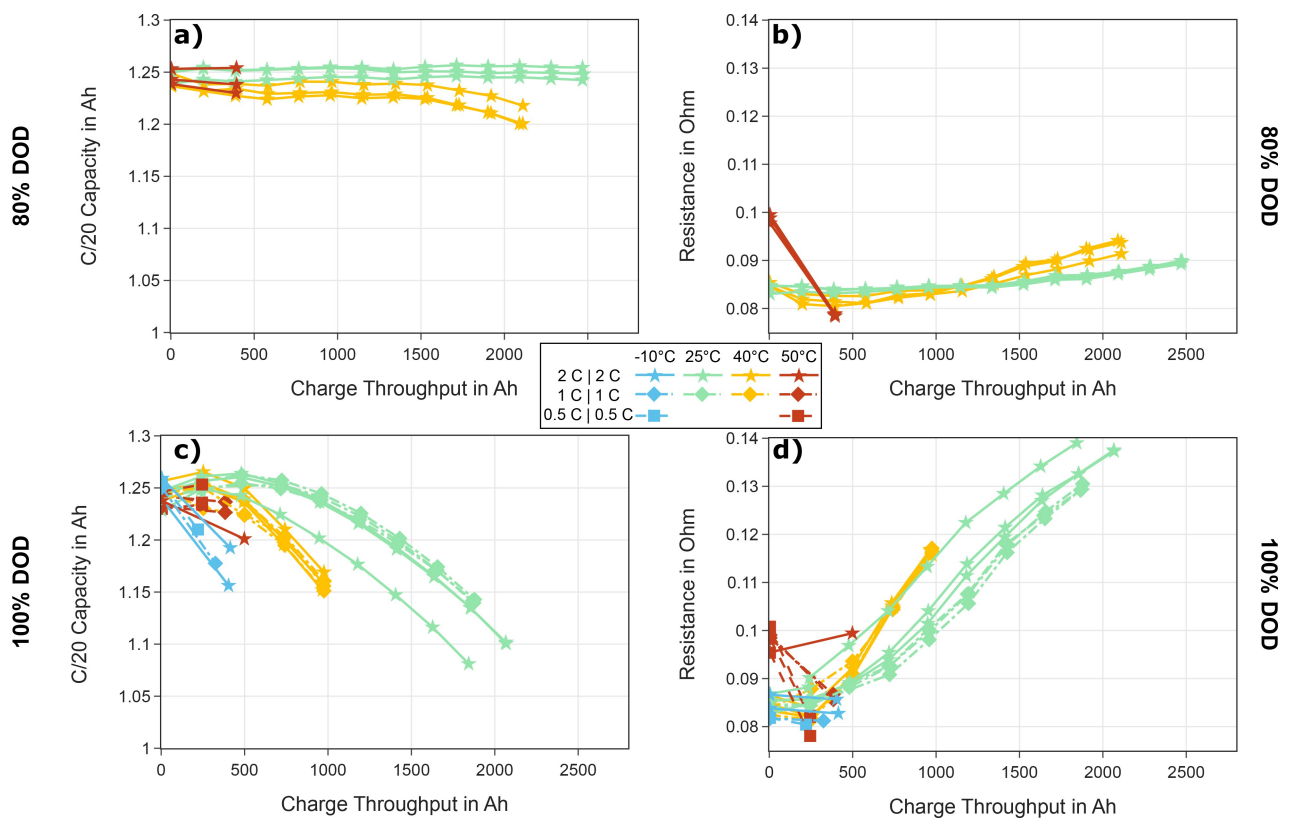


Figure 4. Capacity (left) and resistance (right) trajectories for cells cycled with 80% (top) and 100% DOD (bottom) at various C-rates and temperatures.

were then stopped after their RPT. However, these cells were still operational after a charge throughput of 1870 Ah.

At 40 °C we observed a more rapid capacity decay compared to 25 °C. In this case cells cycled with 1 C and 2 C failed due to the CID after a total charge throughput ranging from 970 to 1170 Ah. In contrast to cells cycled at 25 °C there was no significant difference regarding capacity fade between the cells cycled with different C-rates.

At 50 °C three cells in total stopped due to a triggered CID. As one of those cells was ruptured, releasing its electrolyte, the other cells cycled at 50 °C were stopped for safety reasons. Cells cycled with 2 C exhibit an initial rise of capacity followed by a slight decline of capacity.

Influence of Operating Window on Capacity Fade

In addition to the cells cycled with 100% DOD presented above, cells were also cycled between 3.619 V and 2.029 V (corresponding to about 80% DOD for a new cell, hereafter referred to as 80% DOD). These cycles were conducted with 2 C at -10 °C, 25 °C and 40 °C.

For these lower depths of discharge, we focused on cells cycled at 25 °C and 40 °C, as cells cycled at -10 °C were stopped due to a triggered CID. The capacity loss of cells cycled at 25 °C with 80% DOD was negligible.

At 40 °C cells with 80% DOD exhibited initially stronger capacity fade, followed by a plateau, which bends to lower capacities starting around a charge throughput of 1500 Ah.

Resistance Increase

In this section, we present the resistance increase observed for the different aging conditions investigated in this work.

Our analysis of the pulse resistances R_{pulse} focused on cells cycled at room temperature (Figure 3), 25 °C, and 40 °C (both in Figure 4) as the other cells were stopped early due to a triggered CID and for safety reasons, respectively. The observed trend is similar to the one observed for the capacity fade: resistance increases similarly for cells cycled with 1 C and 2 C with 100% DOD. A difference between those cycled at 40 °C and 25 °C was observed after a charge throughput of 250 Ah: cells at 40 °C exhibited a faster resistance increase coinciding with the accelerated capacity fade (see Figure 4). Cells cycled with 80% DOD exhibited lower resistance rises with very little changes for cells cycled at 25 °C. The resistance of cells cycled at 40 °C with 80% DOD decreased until a total charge throughput of about 400 Ah. After this initial decrease it increased faster compared to the cells cycled at 25 °C.

For cells cycled at room temperature the resistance rise mimicked the capacity fade. Higher discharge rates seem to reduce the resistance increase, similarly to the observed slightly lower capacity fade. Figure 3 shows the trajectory for the

different C-rates tested at room temperature. As with the capacity fade the increased frequency of RPTs and low-rate cycles for the 1 C/1 C-cells of group a (as marked in Figure 3) seems to reduce capacity fade and resistance increase.

CID Triggering

To understand the reasons for the CID triggering we first analyzed the voltage and current values of the specific cells immediately before the CID was triggered (referred to as last voltage and last current, respectively). We then compared the cycling conditions where all cells stopped due to the CID triggering.

The global distribution of last current and last voltage is shown in Figure 5, with the last voltage and last current as x- and y-axis, respectively. The range of the voltage axis represents the voltage window of the full-cell (1.5–3.8 V). The vertical dashed line represents the transition from the sloping region and plateau region of the hard carbon anode based on the fitted half cell data presented in Ref. [7].

The size of the symbol indicates the charge throughput until the CID was triggered. A larger symbol signals an earlier triggering of the CID. Given the approximately linear relation between SOC and voltage, we assumed a rather even distribution of the final voltage if there was no correlation between the operating conditions and the exact time when the CID was triggered. This distribution might be biased towards the end of charge voltage due to the additional time of the CV-phase. In terms of the last current we would expect the respective cycling currents to feature strongly in this plot as cells spent most of the time cycling at these higher C-rates (>C/20). For cells with symmetric rates, we would expect a roughly even distribution between charge and discharge. However, our observation differed from these theoretical assumptions. In terms of the voltage distribution rather low voltages where the cell operates within the sloping region of

the anode are overrepresented compared to the time cells spend at these voltages. Six cells failed at a high SOCs during charge, five of which failed during the CV-phase.

Taking a closer look at operating conditions where all cells failed due to a CID, we found that for all cells cycled at 40 °C and 25 °C with 2 C and 100% DOD the CID was triggered at SOCs below 50%. In all these cases the CID was triggered during a discharge. Of the three cells cycled with 1 C at 40 °C and 100% DOD, two stopped during the rest phase after a RPT while the cell was heated up to 40 °C (at low SOCs), the third one stopped during discharge with an SOC above 50%.

Cells cycled at -10 °C with 80% DOD and 1 C all failed at low or no current and low SOCs. One cell failed during the low C-rate cycles at -10 °C, while two cells failed at the beginning of a cycling period while being cooled down after a RPT.

Degradation Modes Model

In order to better understand the electrochemical behavior of the cell and to be able to diagnose its degradation, the half-cell data was used to build a virtual version of the full-cell using a degradation modes model.^[13] Figure 6 compares the voltage response of the PE (top row), NE (middle row), and the full-cell (bottom row).

Positive Electrode

Looking at the PE first, the given voltage response belongs to NaMnFeNiO₂ with a 111 distribution of the transition metals (MnFeNi layered oxide (MFN), detailed analysis in Ref. [7]) with a plateau between 0–50% SOC and a solid solution above, Figure 6a. Plotting the IC curves, Figure 6b, allows to investigate the electrochemical behavior of the electrode in more details. Starting from the high voltages, the solid solution seemed to be divided into two separate reaction ((1) and (2)). At lower voltages, the phase transformation presents a pretty unique signature with an asymmetric peak in discharge and three peaks in charge with the sharpest one towards the higher voltages. While more investigations are necessary to verify, we believe there is at least two reactions occurring in discharge, (3) and (4). Indeed, since the starting potential of a reaction cannot be higher in discharge than in charge, reaction (3) cannot occur at a lower potential in discharge than that in charge. Since peak (4) in charge clearly started at lower voltages, peak (3) in discharge and peak (4) in charge are unlikely related to the same electrochemical reaction. However, we believe the middle peak observed in charge ((3')) actually corresponds to reaction (3) and is likely related to the communicating vessel effect mentioned earlier. This could be related to different grain size having different kinetics.^[19] This is currently under investigation and will be reported in future work. The DV response, Figure 6c, is relatively featureless with two shoulders of different intensity with no clearly defined peaks.

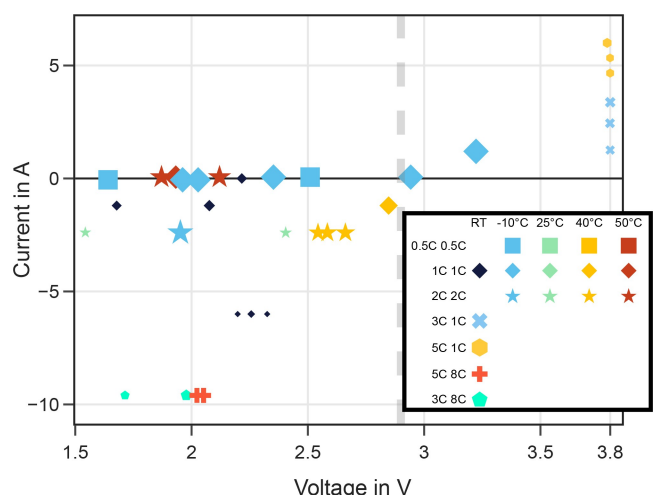


Figure 5. Representation of the last recorded working condition before the CID triggered. The majority of CIDs triggered at lower voltages.

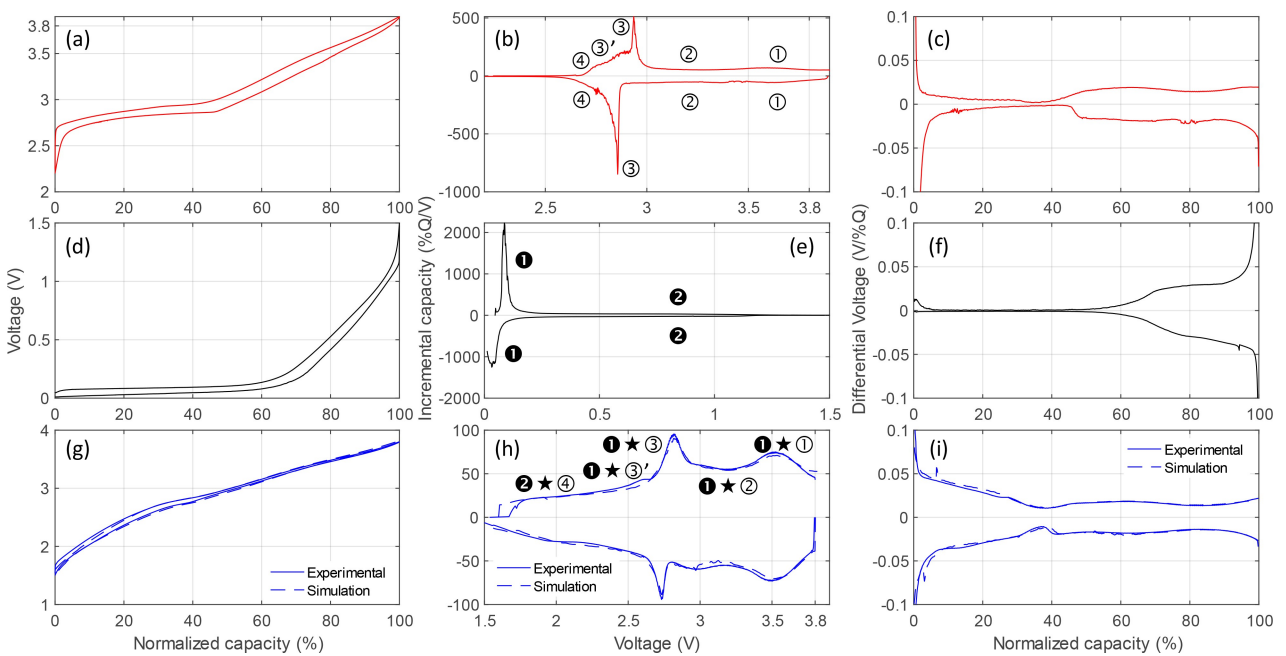


Figure 6. Initial voltage response at C/50 for the PE and NE as well as C/20 for the full-cell with respectively (a, d, g) the voltage vs. normalized capacity, (b, e, h) the incremental capacity, and (c, f, i) the differential voltage responses.

Negative Electrode

The electrochemical response of the NE was found to be consistent with hard carbon (HC),^[7] Figure 6d–f with a plateau up to 60% SOC then a solid solution resulting in a peak and a shoulder on the IC curves and very little features on the DV curves besides a more intense shoulder above 60% SOC.

Full-Cell

Figure 6g–i compares the experimental full-cell response to the emulation obtained from the matching of the half-cell data. Overall, the model was able to replicate the voltage response of the full-cell. From the peak indexation performed on the individual electrodes (Figure 6b and e), the electrochemical features of the full-cell can also be indexed, Figure 6h. Starting from high voltages, the first broad peak corresponds to reaction (1) on the NE occurring at the same time as reaction (1) on the PE. The next shoulder corresponds to reaction (2) on the PE occurring while the NE was still on (1). The most defined peak corresponds to (3) on the PE while the NE remained on (1). This is followed by peak (3)' occurring before the NE transitioned to (2) for the low voltage response of the full-cell where it occurs along (4) on the PE. The model managed to replicate all the features well except for (1)*(3) and (1)*(3)' which ratio of intensity was wrong. While this ratio was shown to vary between cells, the variation observed here is above the level of observed cell-to-cell variations and further investigation are in progress to investigate this issue. It also has to be noted that the best simulations in charge and discharge were not obtained with the same set of parameters. Most notably, the calculated

offset was 6% lower in charge. The origin of this difference is still unclear at this time.

Discussion

Based on the experimental investigations and the results, these are discussed in the following subsections. The discussion starts with the degradation mode analysis (subsection Degradation Mode Analysis), followed by the aging analysis (Subsection Aging Analysis), and ends with the discussion of the CID activation (subsection CID).

Degradation Mode Analysis

With the emulation of the full-cell successful, the virtual cell can be degraded and the prospected impact of the different degradation mode can be assessed,^[13] Figure 7. Since the half-cell data was only collected at rates at or below C/50, only the thermodynamic degradation modes will be discussed in this work. Starting with the loss of sodium inventory (LSI), it is predicted to make peak (1)*(3) completely disappear while shifting towards higher voltage. This is because LSI increased the offset and thus pushed (2) on the NE towards higher voltages. A loss of active material (LAM) on the desodiated PE will result in the increase of the charge initial voltage when the PE becomes limiting as well as a significant sharpening of peak (1)*(3), and a intensity decrease for peaks (1)*(2) and (1)*(1). This is because the contraction of PE allows more of its capacity to occur alongside (1) on the NE. Loss of active material on negative electrode (LAM_{NE}) will also sharpen peak (1)*(3) but in

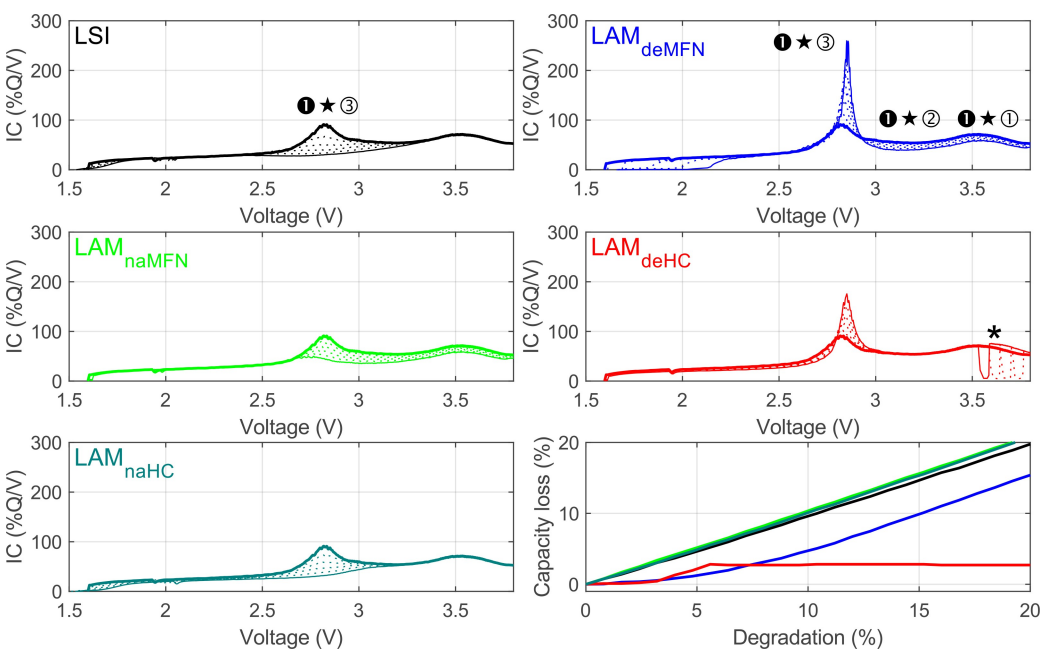


Figure 7. Degradation map for the HC/MFN full-cell with, from top left to bottom right, the impact of up to 20% loss of sodium inventory (LSI), loss of MFN (LAM_{deMFN}), loss of sodiated MFN (LAM_{naMFN}), loss of HC (LAM_{deHC}), loss of sodiated MFN (LAM_{naHC}), and the associated predicted capacity loss. The thick lines represent the initial responses (simulated) and the thin full lines the final ones (after 20% respective loss, simulated). Intermediates in 4% increments are represented by the dotted lines. (*) Since the half-cell data that was used for this work had a cutoff voltage of 10 mV at end of discharge, the apparition of plating at 0 V is accompanied by a sharp drop of potential from the cutoff to 0 V, that is visible on the IC curves. This is an artifact of the simulation and the transition to plating will be far less drastic in real cells.^[23]

a smaller fashion. Sodium plating is also predicted to arise quickly (indicated by * in Figure 7) since the calculated NE/PE loading ratio was rather small (0.95). Losing sodium along the LAMs will tamper their impact on peak (1)*(3) while delaying plating during LAM_{NE} . For loss of active material on positive electrode (LAM_{PE}), the impact on peaks (1)*(2) and (1)*(1) is still visible. Finally, looking at the associated capacity losses, any loss of sodium, whether alone or in the active materials will result in direct capacity loss whereas desodiated LAM_{PE} has an incubation period (while the NE is limiting at end of discharge). LAM_{NE} did not induce any capacity loss as the sodium plating was considered 100% reversible in the simulations. In the case it is not, the capacity will be lost as LSI and not LAM_{NE} .^[20,21] In the light of Figure 7, it can be observed that no degradation mode evolution can actually explain the observed communicating vessel effect between peaks C and D (see section Cell to cell variations), which might indicate that it is inherent to the material itself similarly to what voltage fade would be.^[22]

Aging Analysis

This section discusses the observed degradation occurring under different aging regimes. Cells cycled at -10°C degrade rather fast in terms of the capacity (Figure 4). We attribute this rapid capacity fade to irreversible sodium plating. Interestingly a knee-point is observed for 2 of 3 cells cycled with 0.5 C and 1 C but only for one of three cells cycled with 2 C as shown in Figure S1. This is likely due to the additional heating of the cell

by the increased current at 2 C. All cells cycled at -10°C that exhibited a knee-point stopped due to a triggered CID, whereas the remaining tests were stopped after an initial RPT. At higher temperatures the capacity fade is attenuated. The total charge throughput for cells cycled at 25°C and 2 C until the CID stops the test is over 2000 Ah, equivalent to more than 1600 full cycles (based on the nominal capacity). Further increasing the temperature to 40°C ambient temperature reduces the charge throughput until triggering of the CID to just short of 1000 Ah. Interestingly the capacity fade trajectory is very similar for cells cycled with 1 C compared to those cycled with 2 C at 25°C and 40°C , respectively. This indicates that increased C-rates do not have a detrimental impact on capacity fade and resistance increase within a certain range. However, the earlier triggering of the CID indicates that higher charge currents aggravate other degradation mechanisms such as gassing. As shown in Figure 4 the increase in capacity fade observed for cells cycled with 100% DOD at 25°C and those cycled with 80% DOD at 40°C is preceded by an increase in resistance. It is possible that this would also apply to cells cycled at 40°C with 100% DOD but is omitted by the limited frequency of the RPT.

Cells cycled at room temperature complement these findings: cells operated with charge rates of up to 3 C differ slightly from those charged with 1 C. Increasing the current to 5 C leads to an earlier triggering of the CID.

Considering the relation between capacity fade and resistance increase can be used to compare the mix of aging mechanisms.^[24] A similar gradient in the RC-plane indicates a similar mix of aging mechanisms. Figure 8 shows the capacity

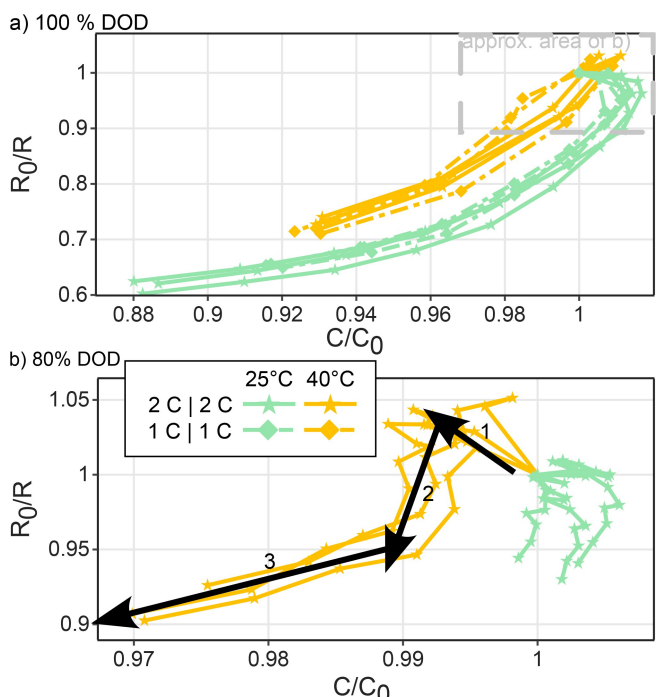


Figure 8. The degradation in the RC-plane. The top panel (a) shows the pathway for cells cycled with 100% DOD. A two-stage process with an initial activation phase (rising capacity for 25 °C and 40 °C, decreasing resistance for 40 °C) is followed by a degradation phase which is similar for the two temperatures. The bottom panel (b) shows the pathway for cells cycled with 80% DOD. A three-section pathway is observed for cells cycled at 40 °C with an initial activation phase with decreasing resistance amid a decrease in capacity (1), followed by a stabilization phase where capacity remains rather constant amid an increasing resistance. The third phase (3) corresponds to the increasing degradation towards the end of the test with decreasing capacity amid continually increasing resistance.

(normalized to the initial capacity C_0) and $\frac{R_0}{R}$, the normalized conductivity of the cell. For cells cycled at 40 °C and 25 °C. This normalization allows for a common starting point of all cells (1,1). Upon resistance increase and capacity fade the respective values decrease, allowing for a simple comparison between the aging conditions. For cells cycled with 100% DOD the curves for both 25 °C and 40 °C show a similar gradient, indicating a similar effect of aging on capacity and resistance for both aging conditions. A difference can be seen in the initial behavior; for cells cycled at 25 °C with 100% DOD an increase of capacity amid a constant resistance is observed, while cells cycled at 40 °C with 100% DOD exhibit a rise in capacity amid a slight decrease of resistance (thus an increase of $\frac{R_0}{R}$). This indicates different initial activation processes.

No notable difference is found between cells cycled with 1 C compared to those cycles with 2 C. Cells cycled at these temperatures with 80% DOD show a slightly more complex behavior: at 40 °C an initial capacity loss is accompanied by a reduced resistance, followed by a phase with rather constant capacity but increasing resistance and a last phase combining capacity fade and resistance increase. At 25 °C the initial behaviour differs with cells shown an initial capacity rise amid fairly constant resistance (similar to cells cycled with 100% SOC). This is followed by a phase with rising resistance (similar

to the second phase observed for cells cycled with 80% DOD at 40 °C). This indicates that there is an initial activation process which is affected by temperature. Afterwards temperature mainly affects the rate of degradation but not the ratio of resistance increase and capacity fade. Thus, we assume similar aging mechanisms albeit at different speed for cells cycled with 40 °C and 25 °C.

The aging studies mentioned in the introduction indicate that cycling-induced degradation was not an issue for these cells.^[8,9] Compared to the cell we investigated in this publication the NVPF-cell has a slightly lower energy density of 83 Wh kg⁻¹.^[9] Cycling with 2 C resulted in a cycle life of about 6000 cycles until 80% remaining capacity, whereas this threshold was reached after roughly 3000 cycles at 1 C. A temperature increase reduced cycle life further to a mere 500 cycles at 40 °C.^[9] When the full capacity is used the cell discussed in this work faces moderate capacity loss in the range of 7% at 40 °C after about 770 equivalent full cycles. Cells cycled at 80% DOD at 40 °C maintain the capacity until the tests are terminated after more than 1600 equivalent full cycles with a total capacity loss below 5%.

Our results show that SIBs can already achieve high cycle life. However a major drawback is the sudden failure observed mainly for cells cycled with 100% DOD due to the CID. A steady capacity fade is advantageous compared to a sudden cell failure in numerous applications as its effect can be mitigated e.g. by developing algorithms which allow aging prediction.^[25] However, the sudden death of a cell due to a triggered CID can be harder to handle.

In order to compare the degradation of the cells under the different conditions in more details using the degradation modes approach, a similar approach than of the one proposed in Ref. [26] can be used with first the determination of which electrode is limiting to establish which mode is responsible for capacity loss, then a study of the most visible change in electrochemical response to assess the other modes. From the calendar and aging data gathered throughout that study, and before the activation of the CID, four categories of degradation were observed, of which one example for each is presented on Figure 9. The first category, Figure 9a encircled both calendar aging experiments as well as the aging with 20% DOD. In that case, the capacity loss is limited and likely induced by LSI. The major changes in the electrochemical response are imputable to the communicating vessel effect between peak C and D that is still unexplained. The second category, Figure 9b, encompassed the testing at 80% DOD and temperatures at and above room temperature. In that case some desodiated LAM_{PE} occurred along side the LSI with a clear increase of peak (1)×(3) and a decrease of peak (1)×(1). Since the NE is still limiting at end of discharge, as the starting potential of the charge did not increase, the capacity loss was induced by LSI despite the up to 10% desodiated LAM_{PE} as estimated from the change of intensity of peak (1)×(1), see Figure 7. The third category, Figure 9c, enclosed the cells tested up to 100% DOD with temperatures room temperature and above. In that case, the desodiated LAM_{PE} is higher (up to 20%) and the PE became limiting at end of discharge after some cycles. This explains the

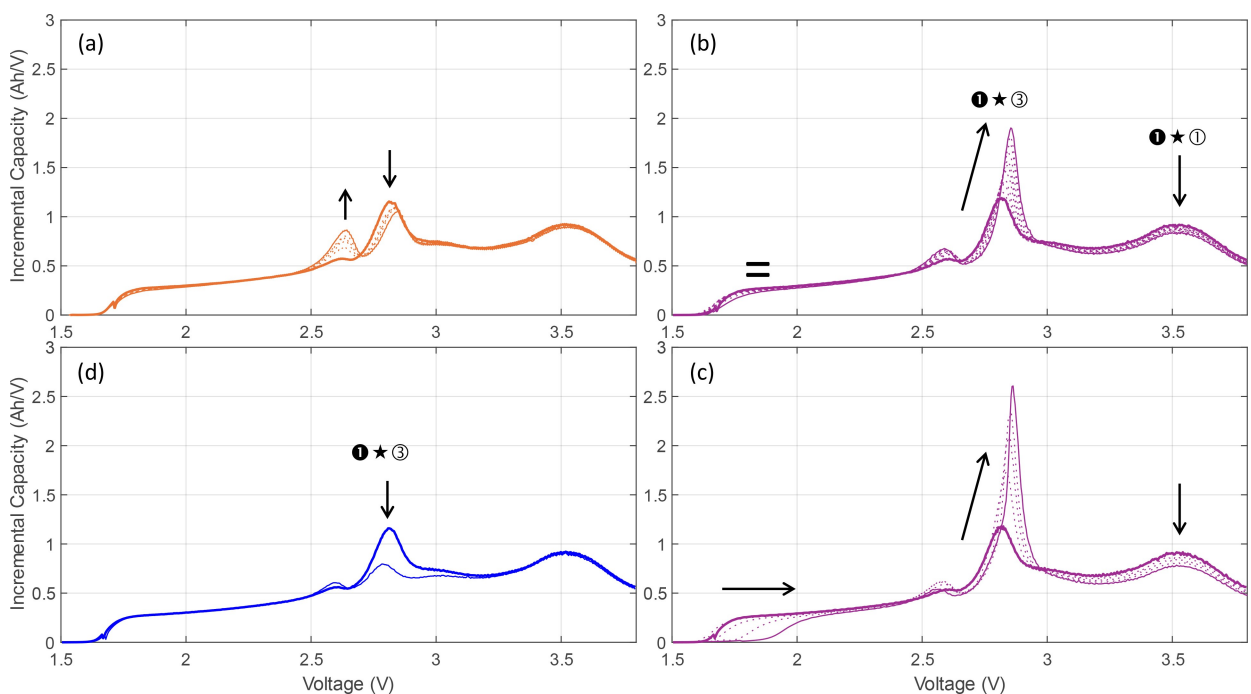


Figure 9. IC curve evolutions for (a) a cell calendar aged at 40 °C and 100% SOC, (b) a cell cycle-aged with 2 C charge and discharge up to 80% DOD at 40 °C, (c) a cell cycle-aged with 2 C cycles up to 100% DOD at 40 °C. The thick lines represent the initial responses and the thin full lines the final ones (last C/20 measurement). Intermediates are represented by the dotted lines, and (d) a cell cycle-aged with 1 C cycles at 100% DOD at -10 °C.

knee observed on the capacity vs. cycle curves Figures 4 and 3 as the capacity loss was first induced by LSI until the PE became limiting. After that, the loss is initiated by desodiated LAM_{PE}. The last category, Figure 9d, included the cells tested at -10 °C. For those, no desodiated LAM_{PE} is detected but a LSI with some desodiated LAM_{NE} as peak (1)•(3) is observed to decrease without moving towards higher voltages. This is in line with what we expect if irreversible sodium plating on the negative electrode is the main aging mechanism at low temperatures.

CID

The CID stopped all but one tests at room temperature. The exception in this case is the cell that exhibits rather rapid abnormal capacity fade. The other testing conditions at different Temperatures where a CID was triggered are listed in Table 2. Each entry represents one cell. Usually, the CID is triggered by increased internal pressure. This internal pressure is likely due to gassing.^[7] Gassing is often connected to side reactions involving the electrolyte as observed for lithium-ion batteries.^[27–29] The electrochemical potentials are more extreme – and thus facilitate side reactions – at higher SOCs, especially during charging with high currents. However, most CIDs were triggered at low SOC, the opposite of the conditions assumed to accelerate gassing reactions.

All cells except eight fail at voltages, where the anode is likely operated in the sloping region at SOCs below 50%. Six of these eight cells underwent aggressive charging with 3 C or 5 C charging current and fail during or just before the CV phase.

For these cells elevated gas-generating side reactions at high SOC can explain the failure. The other two cells are operated at -10 °C and fail at medium voltages. For the remaining 30 cells, which fail at low SOC the failure cannot simply be explained by elevated side reactions due to extreme potentials at anode and cathode, respectively.

Thus, we suggest that gas-consuming reactions might play a role in understanding the gassing issue occurring in these cells. In the scope of lithium-ion battery research CO₂ reduction on the NE has been reported^[30] as a side reaction.

An alternative explanation involves an unstable solid electrolyte interphase (SEI). Certain species within the SEI form at high SOCs (low NE potentials) during charging but become unstable at higher electrochemical potentials (lower SOCs), leading to their decomposition and potentially releasing gaseous species.

Building on these considerations, we propose the following hypotheses, which require further research for validation:

- Gas-consumption: In the sloping region of the hard carbon anode, gas consumption, which occurs within the plateau is suppressed, hence gas released from PE-electrolyte side reactions cannot be consumed resulting in a faster pressure increase within the cell.
- SEI reconfiguration: A dynamic SEI is reconfigured during each cycle and might release gaseous species due to the changing potential at the NE surface. At high SOCs the NE potential does not change hence there is no force that might drive the SEI reconfiguration in these cases.

Testing these hypotheses to identify and mitigate the strong gassing of these SIBs and prolong their service life is

Table 2. Table listing the cells of the non-room temperature cycling experiments which were stopped due to a triggered CID.

Overview of aging conditions

Cell ID	C-rate (ch/dch)	Temperature in °C	DOD in %	Charge Throughput in Ah
S2000FP5HX	2C2C	50.00	100.00	494.17
S2000FNILQ	1C1C	50.00	100.00	379.05
S2000FQ9MI	2C2C	50.00	100.00	493.54
S2000FMK8H	1C1C	40.00	100.00	977.39
S2000FMUJX	1C1C	40.00	100.00	975.56
S2000FNA0F	1C1C	40.00	100.00	1164.49
S2000FLYO2	2C2C	40.00	100.00	1028.06
S2000FMG4P	2C2C	40.00	100.00	1121.32
S2000FN3JX	2C2C	40.00	100.00	989.17
S2000FOCH9	2C2C	25.00	100.00	2222.28
S2000FN8BU	2C2C	25.00	100.00	2120.52
S2000FONCM	2C2C	25.00	100.00	2181.66
S2000FO405	1C1C	-10.00	80.00	79.45
S2000FNG5F	1C1C	-10.00	80.00	69.55
S2000FOQ09	0.5C0.5C	-10.00	100.00	111.94
S2000FQ6K4	0.5C0.5C	-10.00	100.00	124.72
S2000FOSGS	1C1C	-10.00	100.00	77.35
S2000FQ87T	2C2C	-10.00	100.00	94.48
S2000FPFHG	1C1C	-10.00	100.00	101.77
S2000FPM7N	1C1C	-10.00	80.00	98.65

beyond the scope of this work and should be addressed in future studies.

Conclusions

SIBs are regarded as key technology, offering potential solutions to the ecological, economic, and ethical challenges associated with lithium-ion batteries. However, a comprehensive evaluation of the applicability of SIBs requires a thorough investigation into their aging behavior and modes under various environmental conditions. Notably, there is a significant research gap as no extensive aging studies of commercial SIBs have been conducted to date. To fill this research gap, we conduct cyclic and calendar aging tests for 67 commercial SIBs at different temperatures, C-rates, and DODs, aiming to assess aging patterns and degradation modes.

First, we examined the initial cell-to-cell variance across the three key attributes, maximum capacity, rate capability, and polarization, to understand the performance distribution and its implications for future applications. Our findings reveal consistent performance across cells, with all data falling within the 2σ ($\sigma=8$ mAh) interval. Furthermore, we conducted voltage response analyses, employing techniques such as incremental capacity analysis (ICA) and differential voltage analysis (DVA), to evaluate the electrochemical behavior uniformity among cells.

Second, we assessed the capacity fade and resistance increase under various aging conditions. At 25 °C and 2 C

cycling the cells achieved 1600 full cycles. We showed that the aging trajectories, in terms of capacity and resistance, were very similar for 1 C and 2 C cycling, indicating that the cycling rate did not significantly influence aging. Additionally, cells cycled with 100% DOD at both 25 °C and 40 °C show similar degradation gradients, suggesting a consistent aging effect regardless of temperature. However, we observed different initial activation processes at 25 °C and 40 °C, independent of C-rate and DOD. The DOD influences the cells' aging behavior, with 80% DOD substantially reducing degradation. Moreover, we observed rapid capacity fade at -10 °C, which can be attributed to irreversible sodium plating.

Third, we identified the aging modes occurring in the investigated commercial SIB. Using half-cell data, we constructed a virtual model of the full-cell employing a degradation modes model. Our analysis reveals two primary degradation modes: loss of sodium inventory and loss of active material for both the positive and negative electrodes. We observed four categories of degradation, enabling us to determine which electrode is limiting and thereby establish the specific degradation mode responsible for capacity loss. Notably, at high temperatures, the loss of active material on the negative electrode is particularly evident.

Some aging tests were stopped due to gas-induced CID triggering, particularly at low or no current rates and low SOCs. We hypothesize two possibilities to explain the cell gassing under specific aging conditions: One possibility is that this gassing results from the lack of gas consumption on the NE.

Alternatively, it might be caused by the instability of the SEI formed at high SOCs, which becomes unstable at lower potentials and causes gas release.

Our work represents a crucial initial step towards a more in-depth analysis of the aging modes and degradation processes occurring in commercial SIBs. For further analysis, the aging data is made available to the scientific community. In particular, further investigation is needed into the communicating vessel effect, which cannot be explained by the degradation mode evolution. Additionally, our work suggests two hypotheses with regards to the CID triggering that need to be verified in future works.

Author Contributions

S. K. and H. L. contributed equally to this work. **Conceptualization** S. K., H. L. **Methodology** S. K., M. D. **Validation** S. K., C. R., M. D., D. U. S. **Formal Analysis** S. K., M. D. **Investigation** H. L., M. S., B. Q. **Resources** D. U. S. **Data Curation** S. K., M. S., K. L. Q., M. D. **Writing – Original Draft** S. K., H. L., M. S., K. L. Q., M. D. **Writing – Review & Editing** H. L., C. R. **Visualization** S. K., M. D. **Supervision** C. R., M. D., D. U. S. **Project Administration** H. L., C. R. **Funding Acquisition** C. R., M. D., D. U. S.

Acknowledgements

This research received funding from the Federal Ministry of Education and Research (BMBF) (funding code: 03XP0302C (greenBattNutzung)) and the Federal Ministry for Economic Affairs and Climate Action (BMWK) (funding code: 03EI6106D (WINTER)). M. D. is thankful for Office of Naval Research funding, award #N00014-21-1-2250. Open Access funding enabled and organized by Projekt DEAL.

Conflict of Interests

The authors declare no conflict of interest.

Data Availability Statement

All data are available in the main text and Supporting Information. Raw data of the results shown in the main text can be accessed here: 10.18154/RWTH-2024-05745 (accessible after peer-review). All other data are available from the lead contact (H.L.) upon reasonable request.

Keywords: sodium-ion battery • degradation modes • aging analyses • cyclic aging

- [1] E. A. Olivetti, G. Ceder, G. G. Gaustad, X. Fu, *Joule* **2017**, *1*, 229.
- [2] Y.-h. Luo, H.-x. Wei, L.-b. Tang, Y.-d. Huang, Z.-y. Wang, Z.-j. He, C. Yan, J. Mao, K. Dai, J.-c. Zheng, *Energy Storage Mater.* **2022**, *50*, 274.
- [3] L. Yu, T. Liu, R. Amine, J. Wen, J. Lu, K. Amine, *ACS Appl. Mater. Interfaces* **2022**, *14*, 23056.
- [4] G. A. Campbell, *Mineral Economics* **2020**, *33*, 21.
- [5] A. Rudola, A. J. R. Rennie, R. Heap, S. S. Meysami, A. Lowbridge, F. Mazzali, R. Sayers, C. J. Wright, J. Barker, *J. Mater. Chem. A* **2021**, *9*, 8279.
- [6] N. Tapia-Ruiz, A. R. Armstrong, H. Alptekin, M. A. Amores, H. Au, J. Barker, R. Boston, W. R. Brant, J. M. Brittain, Y. Chen, M. Chhowalla, Y.-S. Choi, S. I. R. Costa, M. C. Ribadeneyra, S. A. Cussen, E. J. Cussen, W. I. F. David, A. V. Desai, S. A. M. Dickson, E. I. Eweka, J. D. Forero-Saboya, C. P. Grey, J. M. Griffin, P. Gross, X. Hua, J. T. S. Irvine, P. Johansson, M. O. Jones, M. Karlsmo, E. Kendrick, E. Kim, O. V. Kolosov, Z. Li, S. F. L. Mertens, R. Mogensen, L. Monconduit, R. E. Morris, A. J. Naylor, S. Nikman, C. A. O'Keefe, D. M. C. Ould, R. G. Palgrave, P. Poizot, A. Ponrouch, S. Renault, E. M. Reynolds, A. Rudola, R. Sayers, D. O. Scanlon, S. Sen, V. R. Seymour, B. Silván, M. T. Sougrati, L. Stievano, G. S. Stone, C. I. Thomas, M.-M. Titirici, J. Tong, T. J. Wood, D. S. Wright, R. Younesi, *J. Phys. Energy* **2021**, *3*, 031503.
- [7] H. Laufen, S. Klick, H. Ditler, K. L. Quade, A. Mikitisin, A. Blömeke, M. Schütte, D. Wasylowski, M. Sonnet, L. Henrich, A. Schwedt, G. Stahl, F. Ringbeck, J. Mayer, D. U. Sauer, *Cell Rep. Phys. Sci.* **2024**, *0*.
- [8] M. He, R. Davis, D. Chartouni, M. Johnson, M. Abplanalp, P. Troendle, R.-P. Suetterlin, *J. Power Sources* **2022**, *548*, 232036.
- [9] L. H. B. Nguyen, P. S. Camacho, J. Fondard, D. Carlier, L. Croguennec, M. R. Palacin, A. Ponrouch, C. Courrèges, R. Dedryvère, K. Trad, C. Jordy, S. Genies, Y. Reynier, L. Simonin, *J. Power Sources* **2022**, *529*, 231253.
- [10] M. Dubarry, N. Vuillaume, B. Y. Liaw, *Int. J. Energy Res.* **2010**, *34*, 216, _eprint: <https://onlinelibrary.wiley.com/doi/pdf/10.1002/er.1668>.
- [11] M. Dubarry, G. Baure, *Electronics* **2020**, *9*, 152.
- [12] A. Devie, M. Dubarry, *Batteries* **2016**, *2*, 28.
- [13] M. Dubarry, C. Truchot, B. Y. Liaw, *J. Power Sources* **2012**, *219*, 204.
- [14] D. A. Stevens, J. R. Dahn, *J. Electrochem. Soc.* **2000**, *147*, 1271.
- [15] W. Wang, Y. Gang, Z. Hu, Z. Yan, W. Li, Y. Li, Q.-F. Gu, Z. Wang, S.-L. Chou, H.-K. Liu, S.-X. Dou, *Nat. Commun.* **2020**, *11*, 980.
- [16] X. Xia, J. R. Dahn, *Electrochim. Solid-State Lett.* **2011**, *15*, 1.
- [17] K. Rumpf, M. Naumann, A. Jossen, *J. Energy Storage* **2017**, *14*, 224.
- [18] D. Beck, P. Dechent, M. Junker, D. U. Sauer, M. Dubarry, *Energies* **2021**, *14*, 3276.
- [19] M. Dubarry, J. Gaubicher, D. Guyomard, N. Steunou, J. Livage, N. Dupré, C. P. Grey, *Chem. Mater.* **2006**, *18*, 629.
- [20] M. Dubarry, G. Baure, D. Anseán, *J. Electron. Eng. Conv. Stor.* **2020**, *17*.
- [21] M. Dubarry, D. Beck, *Journal of Power Sources* **2020**, *479*, 228806.
- [22] M.-T. F. Rodrigues, J. Gim, A. Tornheim, O. Kahvecioglu, M. Luo, A. Y. R. Prado, S. E. Trask, J. Croy, D. P. Abraham, *J. Electrochim. Soc.* **2022**, *169*, 040539.
- [23] D. Beck, A. Greszta, A. Roberts, M. Dubarry, Improved Mechanistic Degradation Modes Modeling of Lithium and Sodium Plating **2024**.
- [24] S. Klick, G. Stahl, D. U. Sauer, *Energy Technol.* **2024**, *12*, 2300566, _eprint: <https://onlinelibrary.wiley.com/doi/pdf/10.1002/ente.202300566>.
- [25] K. Honkura, K. Takahashi, T. Horiba, *J. Power Sources* **2011**, *196*, 10141.
- [26] M. Dubarry, D. Anseán, *Front. Energy Res.* **2022**, *10*.
- [27] B. Michalak, H. Sommer, D. Mannes, A. Kaestner, T. Brezesinski, J. Janek, *Sci. Rep.* **2015**, *5*, 15627.
- [28] Z. Mao, M. Farkhondeh, M. Pritzker, M. Fowler, Z. Chen, *J. Electrochim. Soc.* **2017**, *164*, A3469.
- [29] J. Liu, P. Bian, J. Li, W. Ji, H. Hao, A. Yu, *J. Power Sources* **2015**, *286*, 380.
- [30] C. Mao, R. E. Ruther, L. Geng, Z. Li, D. N. Leonard, H. M. I. Meyer, R. L. Sacci, D. L. I. Wood, *ACS Appl. Mater. Interfaces* **2019**, *11*, 43235.

Manuscript received: August 14, 2024

Revised manuscript received: November 25, 2024

Version of record online: January 8, 2025